



Characterization of stress–strain relationships in Al over a wide range of testing temperatures



Tamás Csanádi^a, Nguyen Q. Chinh^{a,*}, Jenő Gubicza^a, György Vörös^a, Terence G. Langdon^{b,c}

^a Department of Materials Physics, Eötvös University Budapest, H-1117 Budapest, Pázmány P. sétány 1/A., Hungary

^b Departments of Aerospace & Mechanical Engineering and Materials Science, University of Southern California, Los Angeles, CA 90089-1453, USA

^c Materials Research Group, Faculty of Engineering and the Environment, University of Southampton, Southampton SO17 1BJ, UK

ARTICLE INFO

Article history:

Received 18 April 2013

Received in final revised form 16 August 2013

Available online 4 September 2013

Keywords:

A. Dislocations

A. Microstructures

A. Strengthening mechanisms

B. Constitutive behavior

B. Stress–strain relationship

ABSTRACT

The stress–strain relationships characterizing plastic deformation of aluminum are described over a wide range of testing temperatures by applying both a widely used phenomenological relationship and a well-known dislocation-based model. It is shown that over the whole range of testing temperatures the trapping of mobile dislocations and the annihilation of forest dislocations are controlled by the same thermally-activated dislocation motion, thereby leading to a simplified model which uses only two parameters to describe the multiplication and the annihilation rates of dislocations. The temperature dependence of these two microscopic quantities is explained. Furthermore, correlations between the characteristics of macroscopic and microscopic descriptions were established over a wide range of testing temperatures for pure Al.

© 2013 Elsevier Ltd. All rights reserved.

1. Introduction

For more than fifty years, considerable interest has been devoted to understanding the plastic behavior of simple face-centered cubic (fcc) metals such as pure aluminum. Thirty years ago, Frost and Ashby (1982) summarized both the theoretical models and experimental data in the form of sets of deformation mechanism maps covering a very wide range of crystalline materials including pure aluminum. These maps divided the flow behavior into a regime of diffusion-controlled creep dominating flow at high temperatures and a regime of thermally-activated flow dominating at low temperatures, thereby suggesting a transition from low to high temperature behavior in the vicinity of $\sim 0.5T_m$, where T_m is the absolute melting point of the material.

On the basis of many different experiments, it is now well established that the work hardening of single crystals may be divided into three distinct stages, designated as I, II and III (Nabarro et al., 1964; Berner and Kronmüller, 1965; Kovács and Zsoldos, 1973; Kocks and Mecking, 2003). Investigations using torsion experiments (Zehetbauer and Seumer, 1993; Zehetbauer, 1993; Les et al., 1997) have suggested the occurrence of two additional stages, denoted as IV and V in the case of polycrystalline metallic materials. Later, applying severe plastic deformation (SPD) techniques, which are favored methods for producing bulk ultrafine-grained materials (Valiev et al., 2000; Valiev and Langdon, 2006; Zhilyaev and Langdon, 2008), it was found that the flow stress tends practically to saturate (Chinh et al., 2004, 2005, 2010; Csanádi et al., 2011) in accordance with the behavior characteristic for stage V. Consequently, it is now possible to investigate the flow process over a wide range of strain at different temperatures and this is important from both a materials science and an engineering point of view.

* Corresponding author. Tel.: +36 1 3722845.

E-mail address: chinh@metal.elte.hu (N.Q. Chinh).

According to the many experimental data, several equations were developed for the description of the stress–strain ($\sigma - \varepsilon$) relationships. There are both phenomenological (Hollomon, 1945; Voce, 1948; Chinh et al., 2004, 2005; Farrokh and Khan, 2009; Csanádi et al., 2011) and dislocation-based (Kocks, 1976; Estrin and Mecking, 1984; Kubin and Estrin, 1990; Malygin, 1990; Lukáč and Balík, 1994; Estrin et al., 1998; Nes, 1998; Barlat et al., 2002; Tóth et al., 2002; Beyerlein and Tomé, 2008; Austin and McDowell, 2011; Fan and Yang, 2011; Gao and Zhang, 2012; Bertin et al., 2013; Hansen et al., 2013; Li et al., 2013) models. In the case of the latter, different microstructural approaches were suggested, including the evolution of the total dislocation density (Kocks, 1976; Estrin and Mecking, 1984; Malygin, 1990; Lukáč and Balík, 1994; Beyerlein and Tomé, 2008, Fan and Yang, 2011), the separate evolution of the mobile and forest dislocations (Kubin and Estrin, 1990; Barlat et al., 2002; Wang et al., 2009; Austin and McDowell, 2011; Gao and Zhang, 2012; Hansen et al., 2013; Li et al., 2013), the separate evolution of the polar and non-polar dislocations (Bertin et al., 2013), the development of the dislocation densities in cell walls and grain interiors (Estrin et al., 1998; Roters et al., 2000; Tóth et al., 2002) and/or the subgrain size and misorientation angle (Nes, 1998) as structural parameters. Recently, the plastic deformation of polycrystals was described also by considering the grain boundary effects (Lim et al., 2011) and the grain size gradient (Li and Soh, 2012) in the case of nanostructured materials. As all of the macroscopic and microscopic models reasonably describe the experimental data, despite their different approaches, there should be a correlation between the main characteristics of these various models. A knowledge of any possible connections would certainly help in achieving a deeper understanding of the mechanisms of plastic deformation, and also it would contribute towards an understanding of the physical meanings of the parameters used in the different models.

This was the motivation for the present work and for the earlier studies reported recently (Chinh et al., 2010; Csanádi et al., 2011). Accordingly, this work may be regarded as a continuation of these recent reports where the room temperature plastic behavior of pure Al and several other fcc metals was studied over a wide range of strain. In these earlier reports (Chinh et al., 2010; Csanádi et al., 2011) the relationships were examined between the parameters of the microscopic processes adopted in the classic Kubin–Estrin (KE) model (1990) and the characteristics of a recent macroscopic description (Chinh et al., 2004). Based on this earlier analysis, the present work is focused on the plastic behavior of pure Al deformed at different testing temperatures. Specifically, the effects of thermal activation are investigated in terms of the temperature dependence of the relevant characteristics of the macroscopic (Chinh et al., 2005) and microscopic KE (Kubin and Estrin, 1990) descriptions. In order to place this report in perspective, the following section provides a brief description of the background to the analysis.

2. Background to the analysis: macroscopic description of the plastic deformation in Al

In an earlier work (Chinh et al., 2005) high purity (99.99%) aluminum samples were deformed by tensile tests over a wide range of temperature between 293 K (room temperature) and 738 K. The specimens were annealed for 30 min. at 673 K to give an initial grain size of $\sim 190 \mu\text{m}$ and then tested using an MTS testing machine operating at a constant cross-head velocity with initial strain rate of $1.0 \times 10^{-3} \text{s}^{-1}$. Additional data were also used in this earlier analysis based on information reported previously for the same material where samples were produced by processing through equal-channel angular pressing (ECAP) (Iwahashi et al., 1998a; Komura et al., 1999). For this purpose, aluminum billets having diameters of 10 mm and lengths of 60 mm were annealed and pressed through a channel at room temperature using a solid die with an angle of 90° between the two parts of the channel and an angle of $\sim 30^\circ$ representing the outer arc of curvature where the two parts of the channel intersect. These internal angles lead to an imposed strain of ~ 1 on each passage through the die. Further details on the principles of processing by ECAP are given in earlier reports (Iwahashi et al., 1996, 1997, 1998b; Furukawa et al., 2001; Valiev and Langdon, 2006) and it is important to note that processing by ECAP provides the opportunity to introduce large strains into the material.

It was demonstrated that the macroscopic stress–strain ($\sigma - \varepsilon$) relationship may be fitted by a phenomenological constitutive relationship of the form (Chinh et al., 2004, 2005):

$$\sigma = \sigma_0 + \sigma_1 \left\{ 1 - \left[\exp - \left(\frac{\varepsilon}{\varepsilon_c} \right)^n \right] \right\} \quad (1)$$

where σ_0 , σ_1 , ε_c and the exponent n are fitting parameters and the strain ε is taken as the absolute amount of plastic strain relative to the annealed state. Physically, the first constant σ_0 , is the friction stress related to the onset of plastic deformation which is then described by the three fitting parameters, σ_1 , ε_c and n . Fig. 1 shows, for example, the experimental $\sigma - \varepsilon$ data obtained at room temperature and a fitted line based on Eq. (1) for two separate situations: very small initial strains as achieved in conventional tensile testing in Fig. 1(a) and a very wide range of strain including the high strains imposed in ECAP in Fig. 1(b) where the datum points represent the individual measured yield stresses. In practice, the flow stress of the specimens subjected to ECAP is documented by reading the 0.2% proof stress, $\sigma_{0.2}$ obtained in the tensile test. This approach is given in Fig. 1(b) where the strain is defined as the sum of that resulting from the tensile test and the imposed strain due to ECAP processing so that a zero strain corresponds to the initial unpressed and annealed condition. The results shown in Fig. 1 confirm the validity of the constitutive relationship given by Eq. (1) and the data in Fig. 1(b) demonstrate a smooth transition from the low strains attained in tensile testing to the high strains imposed through severe plastic deformation. An examination of Eq. (1) shows that, as the flow stress, σ , tends to a saturation value

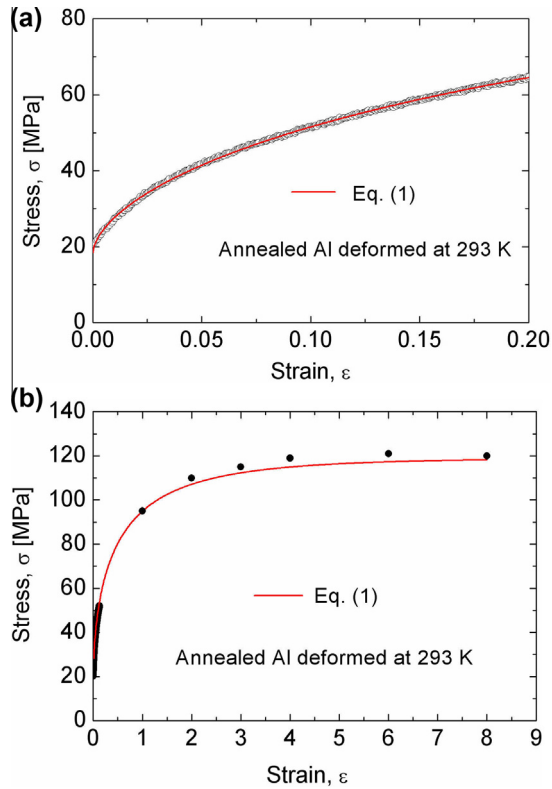


Fig. 1. Experimental stress–strain ($\sigma - \epsilon$) data and a fitted line based on Eq. (1) for (a) low strains and (b) a wide range of strain for pure Al deformed at room temperature (293 K) (Chinh et al., 2005).

$$\sigma_{\text{sat}} = \sigma_0 + \sigma_1 \quad (2)$$

the deformation may be regarded as a steady-state process similar to the flow in the secondary or steady-state stage of creep. At relatively low testing temperatures in the range from 293 to 473 K, the saturation state is attained only at very high strains (i.e., $\sigma \approx 0.95\sigma_{\text{sat}}$, if $\epsilon \geq 2$) so that, for practical purposes at least, the deformation of annealed samples is represented by the work-hardening behavior over the entire range of deformation. Under these conditions, the macroscopic flow stress increases monotonously with increasing strain and this is essentially equivalent to the primary stage in conventional high temperature creep.

An increase in the testing temperature leads to the advent of the secondary stage of creep at relatively small strains. For instance, in Fig. 2 there is a positive stage of work-hardening ($\partial\sigma/\partial\epsilon > 0$) in the early stages of deformation at 623 K (see Fig. 2(a)), whereas there is a maximum flow stress and then a slight decrease in the $\sigma - \epsilon$ curve when data are plotted over the entire range of strain at 623 K as shown in Fig. 2(b). A mathematical analysis shows that, for the real work-hardening stage, the $\sigma - \epsilon$ relationship may be accurately described by Eq. (1) as denoted by the solid lines in Fig. 2(a) and (b). Fig. 2(b) plots both the measured and the fitted data over the entire strain range at 623 K and inspection of this plot shows that the saturation stress ($\sigma_{\text{sat}} = \sigma_0 + \sigma_1$) obtained from fitting the real hardening stage by Eq. (1) practically coincides with the maximum measured value. As already mentioned in the earlier work (Chinh et al., 2005), in the stage of secondary creep, which occurs after the maximum stress, the flow stress is very sensitive to the strain rate and in practice, in tensile testing at constant cross-head velocity, the strain rate decreases slightly with increasing strain leading to a slight decrease in the measured flow stress. In addition, the flow stress may decrease at high temperatures due to the advent of recovery and/or dynamic recrystallization.

Describing the stress–strain relationships by using Eq. (1), the relevant values of the fitting parameters obtained for different testing temperatures are given in Table 1. It is important to emphasize that an approach incorporating Eq. (1) is consistent with the major features of the more conventional and well-established Hollomon-type power law with an exponent n (Hollomon, 1945) and the Voce-type exponential relationship having $n = 1$ (Voce, 1948). Expressing Eq. (1) as a Taylor expansion at small strains leads to

$$\sigma = \sigma_0 + K \cdot \epsilon^n$$

which is the conventional power-law Hollomon relationship where K is a constant. Taking $n = 1$, Eq. (1) leads to the Voce-type exponential equation:

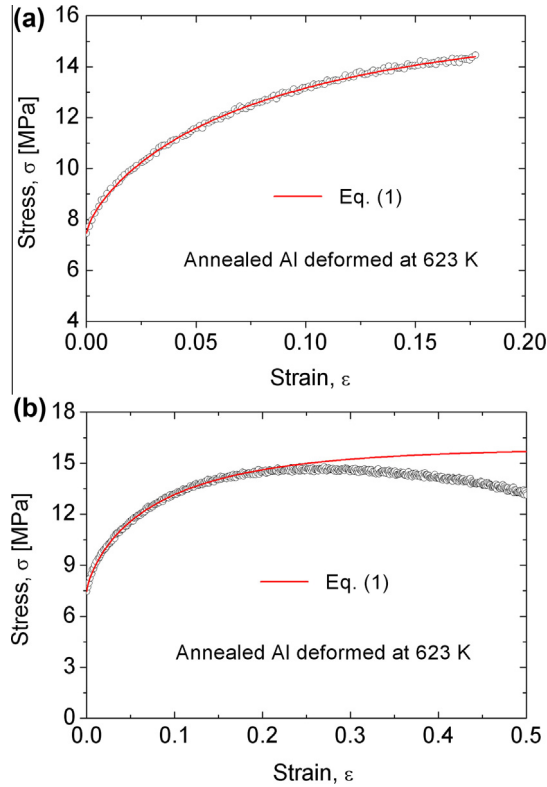


Fig. 2. Experimental stress–strain ($\sigma - \varepsilon$) data and a fitted line based on Eq. (1) for (a) the low strain region of positive work-hardening and (b) the entire range of the experimental strain for pure Al tested at 623 K (Chinh et al., 2005).

Table 1

The values of parameters σ_1 , $\sigma_{sat} = \sigma_0 + \sigma_1$, ε_c and n obtained by fitting Eq. (1) to the stress–strain data obtained on Al deformed at different temperatures, T .

T (K)	σ_1 (MPa)	σ_{sat} (MPa)	ε_c	n
293	108.5	121.2	0.95	0.57
353	95.8	105.9	0.90	0.57
393	73.7	82.9	0.84	0.57
433	61.6	69.9	0.79	0.58
473	49.3	56.5	0.68	0.6
623	8.7	14.2	0.06	0.7
673	5.0	8.7	0.04	0.74
738	4.2	6.3	0.03	0.76

$$\frac{\sigma_{sat} - \sigma}{\sigma_{sat} - \sigma_0} = \exp\left(-\frac{\varepsilon}{\varepsilon_c}\right)$$

where σ_{sat} is the saturation stress given by Eq. (2) ($\sigma_{sat} = \sigma_0 + \sigma_1$).

Fig. 3 shows the temperature dependence of σ_{sat} derived earlier (Chinh et al., 2005) by applying Eq. (1) for pure aluminum over a wide range of testing temperatures (see the values of σ_{sat} in Table 1). Examining the effect of thermal activation on σ_{sat} , it was shown earlier (Chinh et al., 2005) that the temperature dependence of σ_{sat} for pure aluminum over a wide range of testing temperatures can be divided readily into two distinct regions corresponding to a low temperature behavior at $T < 0.5T_m$ and a high temperature behavior at $T > 0.5T_m$. The application of the macroscopic Eqs. (1) and (2) leads, therefore, to the definition of two distinct temperature regimes occurring at low and high temperatures, where the process of plastic deformation can be characterized by different strain rate sensitivities and different activation energies.

In addition, it was shown previously (Chinh et al., 2004) that the macroscopic stress–strain relationship given by Eq. (1) can be supported by considering the effect of microscopic mechanisms of dislocation-based processes. It is well known that the strengthening of pure metals is basically determined by the interaction between dislocations (Chinh et al., 2004, 2010; Csanádi et al., 2011) and the underlying processes of plastic deformation are the formation and the annihilation of dislocations. Considering the rapid development of the cell and/or subgrain structure in deformed metals, both types of dislocation

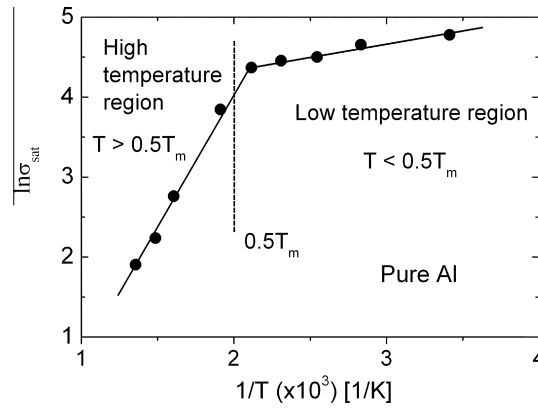


Fig. 3. The regions of low and high temperature flow in pure Al, defined by the Eqs. (1) and (2) (Chinh et al., 2005).

densities, ρ_m for mobile dislocations and ρ_f for forest dislocations, must be incorporated into any analysis in order to provide an accurate description of the development of dislocations during plastic deformation. The average total dislocation density, ρ , is the sum of these two components so that $\rho = \rho_m + \rho_f$. It was showed in earlier studies (Chinh et al., 2004, 2010; Csanádi et al., 2011) that the KE model can be effectively used to describe the development of these dislocation densities in the case of pure fcc metals. Mathematically, the application of this model requires a numerical solution of the following equations:

$$\frac{d\rho_m}{d\varepsilon} = C_1 - C_2\rho_m - C_3\rho_f^{1/2} \quad (3a)$$

and

$$\frac{d\rho_f}{d\varepsilon} = C_2\rho_m + C_3\rho_f^{1/2} - C_4\rho_f \quad (3b)$$

where the terms containing parameters C_i are related to the primary competing microscopic processes occurring during plastic deformation, such as the multiplication of mobile dislocations (C_1), their mutual trapping (C_2), their immobilization through interactions with forest dislocations (C_3) and their annihilation (C_4). The values of the parameters C_i representing the effect of the basic mechanisms for any given material were determined by applying Eqs. (3a) and (3b) so that the stress–strain values deduced from their numerical solution describe best the experimental data (Chinh et al., 2004, 2010; Csanádi et al., 2011). In this analysis the stress is calculated from the total dislocation density by the Taylor equation. Applying the macroscopic description based on Eq. (1) and microscopic description based on Eqs. (3a) and (3b), several plastic features of face-centered cubic Al, Au, Cu and Ni metals deformed at room temperature were discussed - such as the macroscopic stress–strain relationship, the steady state flow, the melting point dependence of the saturation dislocation density and the saturation stress. In the followings the stress–strain relationships obtained at different testing temperatures for pure Al, reported in an earlier work (Chinh et al., 2005) will be characterized by using the KE theoretical model and the corresponding numerical calculation.

3. Microscopic description by the dislocation-based mechanisms

3.1. Investigation of stress–strain relationship

The stress–strain data in the range of real work-hardening ($\partial\sigma/\partial\varepsilon > 0$) obtained for pure Al deformed at different temperatures were also evaluated by the dislocation-based KE model (Kubin and Estrin, 1990). Thus, Eqs. (3a) and (3b) were solved numerically to yield the mobile and forest dislocation densities as a function of strain and the parameters C_i . Then the values of parameters C_i were determined from the best agreement between the experimental flow stress data arising from plastic deformation, $\sigma_p = \sigma - \sigma_0$, and the values calculated from the total dislocation density, $\rho = \rho_m + \rho_f$, using the well-known Taylor equation:

$$\sigma_p = \alpha\mu b(\sqrt{\rho} - \sqrt{\rho_0}) \quad (4)$$

In all cases, the value of the initial dislocation density, ρ_0 , was chosen as $1 \times 10^{11} \text{ m}^{-2}$. In this equation, α is a numerical constant including the Taylor factor ($\alpha = 0.7$ was chosen for all testing temperatures as this value was also used for all fcc metals in the earlier calculations (Chinh et al., 2010; Csanádi et al., 2011)), μ is the temperature-dependent shear modulus having the equation given by Frost and Ashby (Frost and Ashby, 1982) and b is the magnitude of the Burgers vector. It should be noted that in plastically deformed metals usually two strengthening contributions are considered: (i) dislocation strengthening and (ii) grain boundary strengthening. However, it has been shown that each of these two contributions

can be described by a Taylor-type equation as the majority of boundaries in deformed metals are built up from dislocations (Hughes and Hansen, 2000). Thus, in the present study the effect of grain size is also included in the Taylor relationship describing the dislocation–dislocation interactions. The values of parameters C_i obtained from the evaluation of the stress–strain curves are listed in Table 2. It is also noted that the deformation-induced texture may change the value of the Taylor factor, M , thereby influencing the dislocation density determined from the experimental flow stress using the Taylor equation. However, in compressed or ECAP-processed fcc metals the texture is usually weak and this yields only a slight deviation (less than 5% (Gubicza et al., 2008)) of the Taylor factor from the value characterizing the random case (3.06). Thus, the influence of texture on parameters C_i in the KE model is negligible compared to the effect of deformation temperature. The values of parameters C_i now permit an analysis of the roles of individual micro-mechanisms operating during plastic deformation in Al at different testing temperatures.

As an example, Fig. 4(a) plots the mobile, the forest and the total dislocation densities obtained as the best solutions of Eqs. (3a) and (3b) for Al deformed at 623 K. The corresponding microscopic stress–strain curve calculated up to very high strains of 2 is shown in Fig. 4(b) together with the experimental data and the macroscopic stress–strain function obtained from the fitting by using Eq. (1). It is readily apparent from Fig. 4(b) that there is a very good agreement between the experimental data and the macroscopic/microscopic descriptions given by Eq. (1) and Eqs. (3a) and (3b), respectively. In practice, a similar acceptable agreement was obtained in this study for all testing temperatures, thereby providing a confirmation for the basic principles of the KE theoretical model.

Further analysis also shows that, similar to the results obtained for different fcc metals deformed at RT (Csanádi et al., 2011), the coincidence between the experimental and the calculated stress–strain data for Al over a wide range of temperature is sensitive to the values of the parameters C_1 , C_2 and C_4 given in Table 2. It should be noted that during the fitting procedure the best values of the parameters C_i were chosen so that the usual mathematical variance characterizing the usability of the fitting procedure is minimal. Results of the sensitivity analysis show that when the value of the minimal variance is changing within 1%, the values of C_2 and C_4 are almost the same. A relative difference higher than 20% between these two parameters will lead to a drastic increase of the variance, confirming that the coincidence of the coefficients C_2 and C_4 is genuine. By contrast, the determination of the parameter C_3 is accompanied by high uncertainty, as the simulation results change only slightly over a wide range for this parameter. The low sensitivity on the value of C_3 is a consequence of the fact that, at every testing temperature, the value of the term $C_3\rho_f^{1/2}$ is about two orders of magnitude lower than any other term in Eq. (3a) or Eq. (3b). This is demonstrated directly in Fig. 5 for the sample deformed at 623 K. Thus, $C_3\rho_f^{1/2} \ll C_2\rho_m$ and $C_3\rho_f^{1/2} \ll C_4\rho_f$ so that the result means that during the plastic deformation of Al over a wide range of temperature the reduction in the mobile dislocation density can be attributed mainly to the trapping due to the interaction between mobile dislocations (by the term $C_2\rho_m$) rather than to the mobile–forest interaction. Furthermore, the results of the numerical calculations applying Eqs. (3a) and (3b) (see Table 2) also show that the values of the parameters C_2 and C_4 agree within the experimental error for all testing temperatures, similar to other fcc metals deformed at RT (Csanádi et al., 2011).

As was mentioned earlier, many different dislocation-based models are available in the literature, which – despite their different approaches – reasonably describe the experimental data in different stages of plastic deformation by calculating the total (ρ) dislocation density. The treatment of the dislocation components, however, still remains an open question. Concerning the dislocation densities numerically calculated in this work, Fig. 6 shows the ratios (R) of mobile to forest density obtained for some testing temperatures. It can be seen that at low strains ($\varepsilon < 0.1$) the ratio R obtained for room temperature is higher than 10 (see Fig. 6(a)), showing that the mobile dislocation density represents a major fraction of the total density. This result is similar to that obtained through numerical calculation by Bertin et al. (Bertin et al., 2013), or that obtained through the discrete dislocation dynamic (DDD) simulations of (Wang et al., 2009) for single crystals. The evolution of microstructure at low strains – in stages I–III – can be understood if we consider the deformation process starting from the well-annealed state having a low initial dislocation density. The work done by plastic deformation is mainly associated with the creation of new (mobile) dislocations (for instance, by the term C_1 in Eq. (3a)), leading to a higher fraction of the mobile to total densities. In the later stages of the plastic deformation, the fraction of the forest dislocation density governed by Eq. (3b) is enhanced with increasing mobile density, resulting in a decrease of the ratio R which is, together with both dislocation components, eventually saturated at high strains (see Fig. 6(b)).

Table 2

The values of C_i parameters in Eqs. (3a) and (3b) determined by simulations of the experimental stress–strain curves obtained on Al deformed at different temperatures, T .

T (K)	C_1 (1/m ²)	C_2	C_3 (1/m)	C_4
293	2.33×10^{14}	1.1	4×10^5	1.2
353	2.01×10^{14}	1.3	5×10^5	1.4
393	1.34×10^{14}	1.4	4×10^5	1.4
433	1.00×10^{14}	1.4	4×10^5	1.5
473	8.14×10^{13}	1.6	3×10^5	1.7
623	4.54×10^{13}	21	3×10^5	21
673	3.15×10^{13}	31	3×10^5	32
738	2.91×10^{13}	36	2×10^5	37

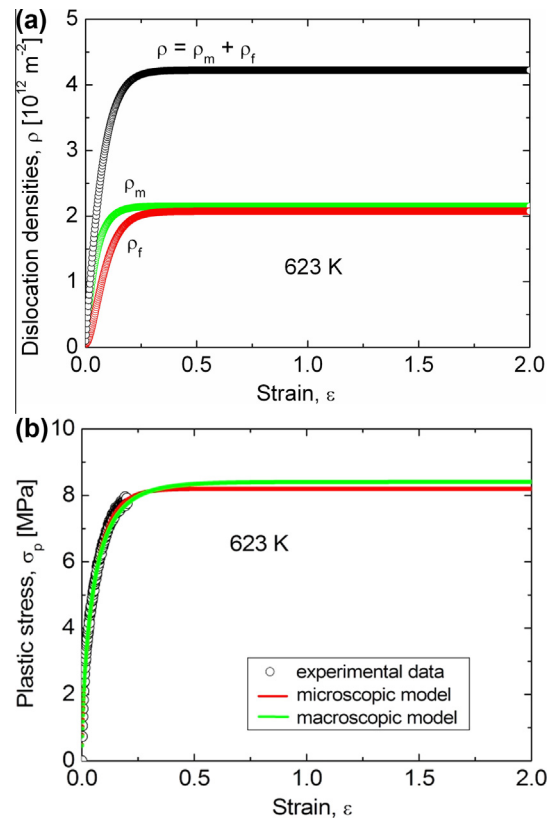


Fig. 4. The solution of Eq. (3) for the testing temperature of 623 K, showing (a) the evolution of the dislocation densities with strain and (b) the corresponding numerically calculated stress–strain curve together with the experimental data and the corresponding fitted function based on Eq. (1) over a wide range of strain.

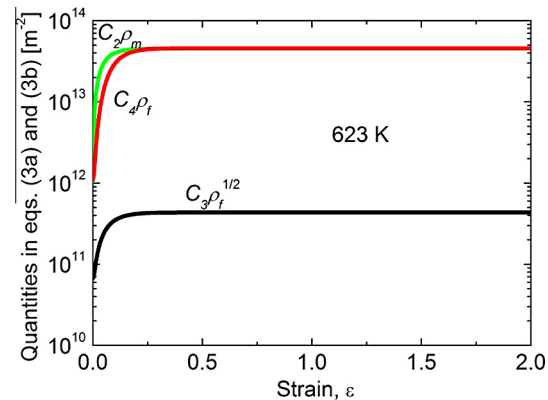


Fig. 5. The quantities of $C_2\rho_m$, $C_4\rho_f$ and $C_3\rho_f^{1/2}$ numerically calculated for a testing temperature of 623 K as a function of strain, demonstrating their contributions in Eqs. (3a) and (3b).

The saturation of other kinds of dislocation components, as with the dislocation densities in cell walls and grain interiors (Estrin et al., 1998; Roters et al., 2000) calculated for the analysis of the slip resistance at high strains including the stages III–V, is also well-established in the description of the plastic deformation of different cell/subgrain-forming metals and alloys. It should be noted that in this case the component (cell wall and cell interior) dislocation densities are defined for different volume fractions of the samples, being rather local dislocation densities inside the cell wall and inside the cell interior, respectively. As the fraction of the cell wall, f_w is generally low, f_w may decrease from 0.25 to only 0.05 (Estrin et al., 1998), and the local cell wall (immobile) dislocation density may be much higher than the cell interior (mobile) density which is defined for a much higher volume fraction.

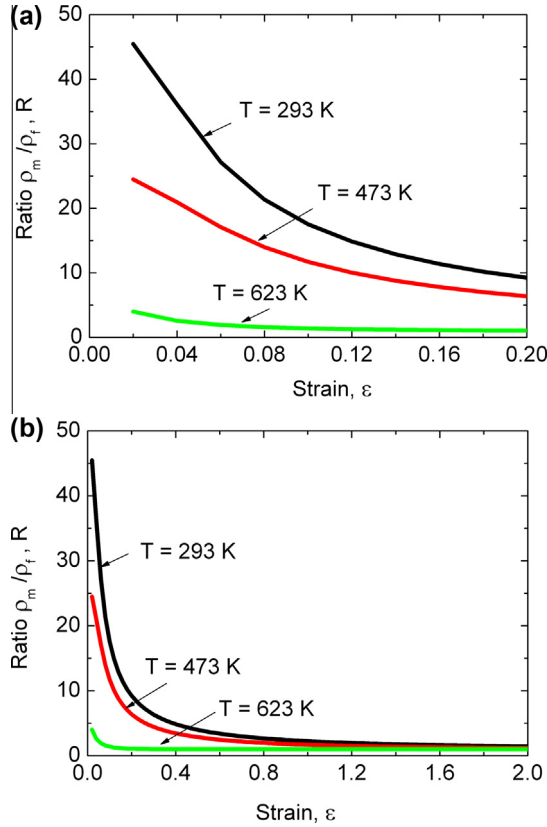


Fig. 6. The ratios R of the mobile to forest dislocation densities numerically calculated by Eqs. (3a) and (3b) for some testing temperatures a) at low strains and b) over a wide range of strains.

Considering the mentioned features of the numerical solutions, Eqs. (3a) and (3b) of the KE model can be simplified for Al over a wide range of testing temperature, as they were already simplified for other fcc metals deformed at RT (Csanádi et al., 2011). Briefly, in the first step, neglecting the term $C_3\rho_f^{1/2}$, Eqs. (3a) and (3b) can be simplified as:

$$\frac{d\rho}{d\varepsilon} = C_1 - C_2\rho_m \quad (5a)$$

and

$$\frac{d\rho_f}{d\varepsilon} = C_2\rho_m - C_4\rho_f, \quad (5b)$$

respectively. Considering the saturation state at high strains, where the mobile and forest dislocation densities are saturated to $\rho_{m,sat}$ and $\rho_{f,sat}$, respectively, and from Eq. (5b)

$$\frac{d\rho_{f,sat}}{d\varepsilon} = C_2\rho_{m,sat} - C_4\rho_{f,sat} = 0 \quad (6)$$

we get

$$\frac{\rho_{m,sat}}{\rho_{f,sat}} = \frac{C_4}{C_2} \quad (7)$$

The similarities in values of C_2 and C_4 (Table 2) results in similar saturation densities for the forest and mobile dislocations. It has been shown for several fcc metals deformed at RT that the similar values of C_2 and C_4 suggest that both the trapping of mobile dislocations and the annihilation of forest dislocations are controlled by the same thermally activated dislocation motion (Csanádi et al., 2011).

In addition, there are some further important consequences of the simplification of the KE model. Starting from the total dislocation density $\rho = \rho_m + \rho_f$, we get:

$$\frac{d\rho}{d\varepsilon} = \frac{d\rho_f}{d\varepsilon} + \frac{d\rho_m}{d\varepsilon} = C_1 - C_4\rho_f \quad (8)$$

Table 3

The values of parameters C_1 and C_4 and ρ_{sat} determined by Eq. (13) of the simplified KE model applied for the experimental stress–strain curves obtained on Al deformed at different temperatures.

T (K)	C_1 (1/m ²)	C_4	ρ_{sat} (1/m ²)
293	2.33×10^{14}	1.15	4.03×10^{14}
353	2.01×10^{14}	1.32	3.05×10^{14}
393	1.34×10^{14}	1.40	1.91×10^{14}
433	1.02×10^{14}	1.43	1.43×10^{14}
473	8.13×10^{13}	1.66	9.80×10^{13}
623	4.54×10^{13}	21.0	4.33×10^{12}
673	3.16×10^{13}	31.7	1.99×10^{12}
738	2.93×10^{13}	36.3	1.61×10^{12}

Differentiating this equation with respect to ε leads to:

$$\frac{d^2 \rho}{d\varepsilon^2} = -C_4 \frac{d\rho_f}{d\varepsilon} \quad (9)$$

Substituting Eq. (5b) into Eq. (9) we get:

$$\frac{d^2 \rho}{d\varepsilon^2} = -C_4(C_2\rho_m - C_4\rho_f) \quad (10)$$

Using the relationships $\rho_m = \rho - \rho_f$ and $C_4\rho_f = C_1 - \frac{d\rho}{d\varepsilon}$, Eq. (10) can be rewritten as:

$$\frac{d^2 \rho}{d\varepsilon^2} = -C_4 \left[C_2(\rho - \rho_f) - C_1 + \frac{d\rho}{d\varepsilon} \right] = -C_2C_4\rho + C_2C_4\rho_f + C_1C_4 - C_4 \frac{d\rho}{d\varepsilon},$$

or

$$\frac{d^2 \rho}{d\varepsilon^2} = -C_2C_4\rho + C_2 \left(C_1 - \frac{d\rho}{d\varepsilon} \right) + C_1C_4 - C_4 \frac{d\rho}{d\varepsilon} \quad (11)$$

Re-arranging Eq. (11) leads to a second-order differential equation for the total dislocation density, ρ :

$$\frac{d^2 \rho}{d\varepsilon^2} + (C_2 + C_4) \frac{d\rho}{d\varepsilon} + C_2C_4\rho - C_1(C_2 + C_4) = 0, \quad (12)$$

in which the role of parameters C_2 and C_4 is symmetrical. Considering the results of numerical simulation based on the experimental data (see Table 2), it is reasonable to take the parameters C_2 and C_4 as equal ($C_2 = C_4$). In this case, Eq. (12) can be expressed simply as:

$$\frac{d^2 \rho}{d\varepsilon^2} + 2C_4 \frac{d\rho}{d\varepsilon} + C_4^2\rho - 2C_1C_4 = 0, \quad (13)$$

which has analytical solution given by the following closed form:

$$\rho(\varepsilon) = \frac{2C_1}{C_4} - \left(\frac{2C_1}{C_4} - \rho_0 \right) \left(1 + \frac{C_4\varepsilon}{2} \right) \exp(-C_4\varepsilon), \quad (14)$$

where ρ_0 is the initial dislocation density at $\varepsilon = 0$ ($\rho(0) = \rho_0$). As mentioned earlier, this value is taken as $1 \times 10^{11} m^{-2}$ at every testing temperature for the best solutions in the present analysis. In the solution of Eq. (13) the initial value of the first derivative of ρ is given by Eq. (8) as $\rho'(0) = C_1 - C_4\rho_f(0)$ and as a first approximation, it is reasonable to take $\rho_m(0) = \rho_f(0) = \frac{\rho_0}{2} = \frac{\rho_0}{2}$ in every calculation (here the ratio $\rho_m(0)/\rho_f(0) = 1$). The results of the present analysis would change within only 2% if the ratio $\rho_m(0)/\rho_f(0)$ changed between 0.1 and 10). Applying the analytical solution Eq. (14), the values of parameters C_1 and C_4 determined by the simplified KE model are listed in Table 3. It can be seen that they are only slightly different from the values obtained using the original KE model as given in Table 2. As an example, Fig. 7 compares the total dislocation densities obtained from the KE model and the simplified KE model using Eqs. (3a,3b) and (4), respectively, for Al deformed at 293 K, 473 K and 623 K. The good agreement between the dislocation densities gives a clear confirmation of the validity of the simplified KE model. It should be emphasized that the expected maximum dislocation density, ρ_{max} , can be calculated from these equations. The values of ρ_{max} and the parameters C_1 and C_4 in Eq. (4) are strongly affected by the testing temperature, as can be seen in Table 3.

3.2. Relationships between the characteristics of the macroscopic and microscopic descriptions

Considering Eq. (12) for the total dislocation density and its analytical solution given in Eq. (13), the flow stress increment produced by the plastic strain ($\sigma_{p,cal}$) can be calculated using Eq. (4) as:

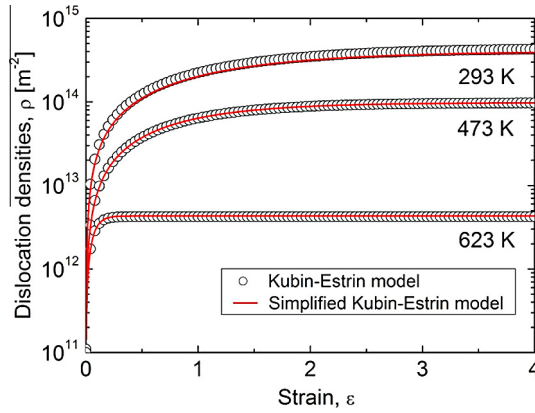


Fig. 7. The evolution of the total dislocation densities calculated by the Kubin–Estrin and the simplified Kubin–Estrin models for some different temperatures, showing the validity of the simplification and also the strong temperature dependence of the saturation dislocation density, ρ_{\max} .

$$\sigma_{p,cal}(\varepsilon) = \alpha \cdot \mu \cdot b \cdot \left\{ \sqrt{\frac{2C_1}{C_4} - \left(\frac{2C_1}{C_4} - \rho_0\right) \left(1 + \frac{C_4\varepsilon}{2}\right) \exp(-C_4\varepsilon) - \sqrt{\rho_0}} \right\} \quad (15)$$

which is affected also by the microscopic processes, characterized by C_1 and C_4 parameters, of plastic deformation. The strain dependence of this flow stress increment, $\sigma_{p,cal}$ produced by the plastic strain allows us to correlate it to the corresponding strain-dependent term, the second term, in the phenomenological Eq. (1):

$$\sigma_{p,phen}(\varepsilon) = \sigma_1 \left\{ 1 - \exp \left[- \left(\frac{\varepsilon}{\varepsilon_c} \right)^n \right] \right\} \quad (16)$$

which is determined by the macroscopic parameters σ_1 , ε_c and n . Making Eqs. (15) and (16) equal at high strains ($\varepsilon \rightarrow \infty$) leads to:

$$\sigma_1 = \alpha \cdot \mu \cdot b \cdot \left(\sqrt{\frac{2C_1}{C_4} - \sqrt{\rho_0}} \right) \quad (17)$$

which reflects quantitatively that the maximum strength attainable during plastic deformation is determined unambiguously by the multiplication and annihilation of dislocations over a wide range of testing temperatures. Investigating the equality of Eqs. (15) and (16) at $\varepsilon = \varepsilon_c$, we get:

$$\alpha \cdot \mu \cdot b \cdot \left\{ \sqrt{\frac{2C_1}{C_4} - \left(\frac{2C_1}{C_4} - \rho_0\right) \left(1 + \frac{C_4\varepsilon_c}{2}\right) \exp(-C_4\varepsilon_c) - \sqrt{\rho_0}} \right\} = \sigma_1 \left(1 - \frac{1}{e}\right),$$

and substituting the value of σ_1 by the formula given in Eq. (17) yields

$$\sqrt{\frac{2C_1}{C_4} - \left(\frac{2C_1}{C_4} - \rho_0\right) \left(1 + \frac{C_4\varepsilon_c}{2}\right) \exp(-C_4\varepsilon_c) - \sqrt{\rho_0}} = \left(\sqrt{\frac{2C_1}{C_4} - \sqrt{\rho_0}} \right) \left(1 - \frac{1}{e}\right) \quad (18)$$

Dividing both sides of Eq. (18) by $\sqrt{\frac{2C_1}{C_4}}$, taking the value of the ratio $\rho_0/\left(\frac{2C_1}{C_4}\right)$ between 10^{-2} and 10^{-3} , as well as the value of its square root between 10^{-1} and 3×10^{-2} , the value of the quantity $C_4\varepsilon_c$ can be obtained between 0.88 and 1.01 for different testing temperature. It is reasonable to approximate the product of $C_4\varepsilon_c$ by one, so that

$$\varepsilon_c \approx \frac{1}{C_4} \quad (19)$$

Both the Eqs. (17) and (19) represent useful relationships between the characteristics of macroscopic description by Eq. (1) and microscopic description given by Eqs. (3a) and (3b). Fig. 8 shows the relationship between the quantities $\frac{\sigma_1}{\alpha \cdot \mu \cdot b}$ and $\sqrt{\frac{2C_1}{C_4} - \sqrt{\rho_0}}$ (Fig. 8(a)) as well as between the quantities ε_c and $\frac{1}{C_4}$ (Fig. 8(b)) for different testing temperatures, for which the value of σ_1 and ε_c , and that of C_1 and C_4 are listed in Tables 1 and 3, respectively. The datum points in both figures are fitted well by straight lines which go through the origin. The slopes of ~ 1 in both Fig. 8(a) and (b) unambiguously confirm the validity of Eqs. (17) and (19) describing the relationships between the characteristics (σ_1 , ε_c) of the macroscopic description and (C_1 , C_4) of the microscopic mechanisms. Eqs. (17) and (19) also mean that the values of C_1 and C_4 can be estimated from σ_1 and ε_c , respectively, for pure Al deformed at different testing temperatures.

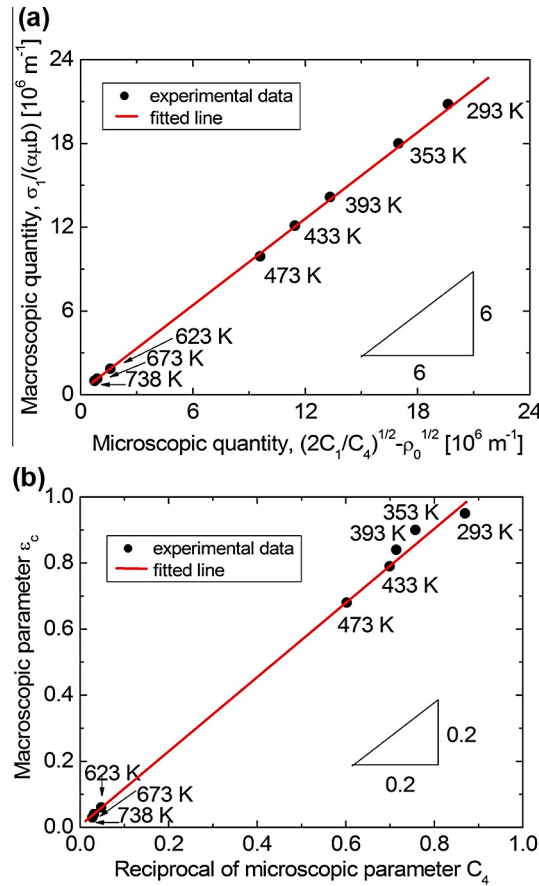


Fig. 8. The relationship between the characteristics of macroscopic and microscopic descriptions as (a) $\frac{\sigma_i}{\alpha \mu b}$ versus $(\sqrt{\frac{2C_1}{C_4}} - \sqrt{\rho_0})$ and (b) ϵ_c versus $\frac{1}{C_4}$ for different testing temperatures.

3.3. The temperature dependence of the microscopic mechanisms

As already noted, the experimental and numerical results (given in Table 3) show that the quantities ρ_{sat} , C_1 and C_4 are strongly temperature-dependent. As ρ_{sat} is closely related to σ_{sat} via the Taylor formula, the natural logarithm of the saturation dislocation density versus the reciprocal of the testing temperature ($1/T$) is plotted in Fig. 9(a). The datum points in Fig. 9(a) can be divided into two distinct groups corresponding to low and high temperatures, respectively. The transition between the two regions occurs at a temperature of 473–483 K (200–210 °C), equivalent to a homologous temperature of ~ 0.51 – $0.52T_m$, where T_m is the absolute melting temperature of Al. Considering the Taylor formula in Eq. (4), the $\ln \rho_{sat} - 1/T$ function obtained in the present work corresponds to the $\ln \sigma_{sat} - 1/T$ plot shown in Fig. 3, reported in an earlier work (Chinh et al., 2005). It is well-known that in the high temperature region ($T > 0.5T_m$) the plastic deformation in Al is controlled mainly by self-diffusion having an activation energy of about 130–140 kJ/mol (Frost and Ashby, 1982; Chinh et al., 2005), whilst the annihilation of dislocations in the saturation state at low temperatures ($T < 0.5T_m$) occurs instead by pipe diffusion and/or grain boundary diffusion and has a much lower activation energy of about 82–84 kJ/mol (Frost and Ashby, 1982; Chinh et al., 2006). This difference in the activation energies lead to the low and high temperature regions of the ρ_{sat} . It should be noted that the difference in the slopes of the two fitted straight lines in Fig. 9(a) do not reflect directly the difference in the activation energies in the two temperature regimes as the slopes are also affected by the strain rate sensitivity parameter (Chinh et al., 2005, 2006). The larger slope in the high temperature regime is caused by both the larger activation energy and the larger strain rate sensitivity parameter.

According to Eq. (14) the saturation dislocation density can be expressed by C_1 and C_4 as $\rho_{sat} = \frac{2C_1}{C_4}$. Therefore, the temperature dependence of C_1 and C_4 determine the variation of ρ_{sat} as a function of temperature. Fig. 9(b) plots the values of parameters C_1 and C_4 as a function of temperature, T . Different tendencies can be observed as the multiplication of dislocation (C_1) is decreasing while the annihilation of dislocation (C_4) is increasing with increasing testing temperature. These trends are in accordance with the model proposed previously for an explanation of the results obtained by the KE evaluation procedure (Csanádi et al., 2011). This simple model was already applied successfully for the interpretation of the similar values of C_2 and C_4 and the negligible magnitude of $C_3\rho_f^{1/2}$ compared to other terms in the KE equations (Csanádi et al., 2011). In

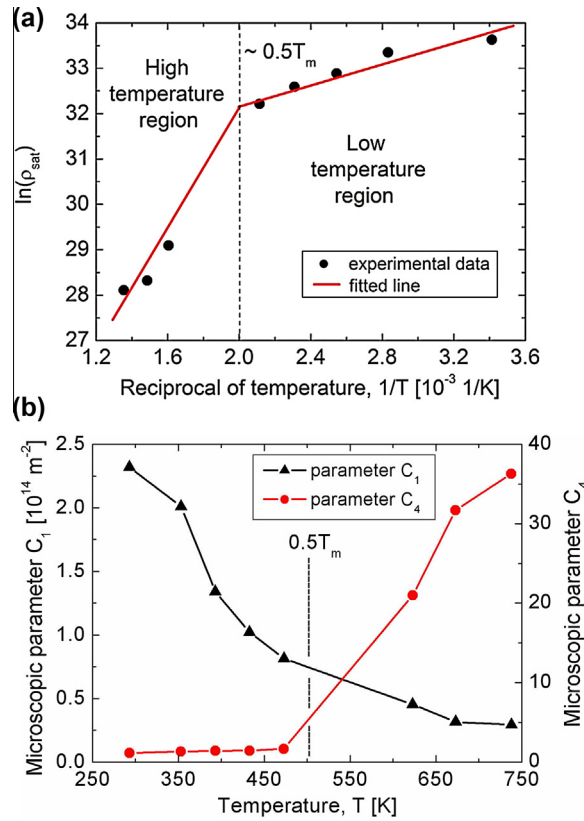


Fig. 9. The temperature dependence of (a) the saturation dislocation density, ρ_{sat} (b) the C_1 parameter characterizing dislocation multiplication and the C_4 parameter characterizing dislocation annihilation.

this model, the mobile dislocations multiply at jogs which are formed due to the intersection of dislocations by other dislocations gliding on non-coplanar planes, as illustrated in Fig. 10, where the jog is indicated by a thick dotted line. Our model is in accordance with previous studies (e.g. Hsiung and Lassila, 2002) which have revealed that in pure metals the jogs formed on screw dislocations act as the most important dislocation multiplication sources when deformed under quasi-static conditions. Most probably, this mechanism remains dominant even for large dislocation densities. In Fig. 10 the direction and the length of the jog formed on the first dislocation gliding in plane S_1 correspond to the Burgers vector of the other dislocation. Usually the slip plane of the jog does not lie in the moving direction of the gliding segments in planes S_1 and S_2 and therefore the jog can follow these segments only through a non-conservative motion. Due to the difficulty of this motion, the jog falls behind the gliding segments and, as a result, the two gliding segments bow out in planes S_1 and S_2 , yielding an in-

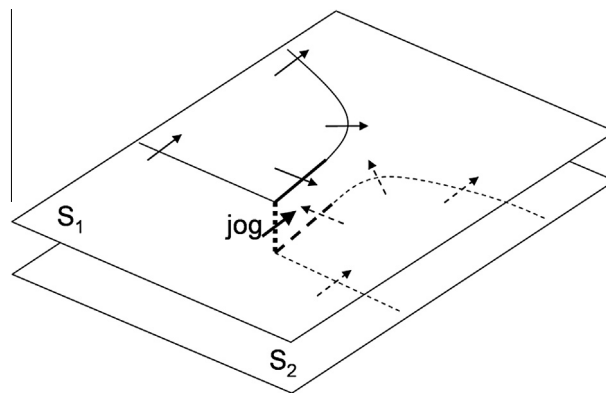


Fig. 10. A schematic illustration showing the multiplication of mobile dislocations and their trapping at a jog formed by intersection of mobile dislocations gliding on non-coplanar planes.

crease in the mobile dislocation density. With increasing temperature, the climb of the jog becomes easier due to more rapid vacancy diffusion, and therefore the lagging of the jog behind the gliding segments is reduced and the length of the newly formed mobile dislocations decreases. The lower rate for the formation of mobile dislocations at the higher temperature is reflected in the lower value of C_1 .

In this model the forest dislocations are formed by trapping the mobile dislocation segments with opposite signs gliding in planes S_1 and S_2 in the vicinity of the jog. These segments in Fig. 10 are illustrated by thick solid and dashed lines. There is an attractive interaction between these segments and they can move towards each other by thermally-activated mechanisms such as climb to form an immobile dipole. Later, these dislocation segments are annihilated by the same mechanism, which leads to the close values of C_2 and C_4 . With increasing temperature, the easier occurrence of the thermally-activated processes yields a faster trapping and annihilation of dislocations, leading to larger values of C_4 .

Fig. 9(b) reveals that in the low temperature regime ($T < 0.5T_m$) the temperature dependence of parameter C_4 is much weaker than that for parameter C_1 . At the same time, at high temperatures ($T > 0.5T_m$) parameter C_4 shows a strong sensitivity to temperature variation. As $\rho_{sat} = \frac{2C_1}{C_4}$, therefore the temperature dependence of ρ_{sat} is determined mainly by the formation of mobile dislocations (C_1), and the annihilation of forest dislocations (C_4) in the low and high temperature regimes,

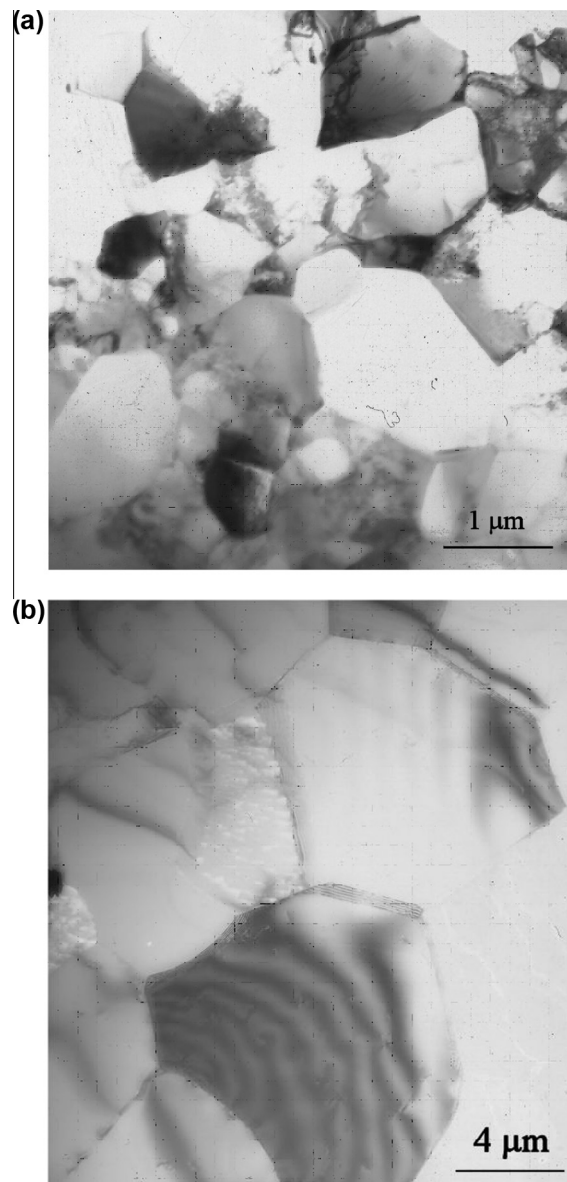


Fig. 11. Microstructures of pure Al after processing by ECAP at room temperature to a strain of ~ 8 (a) remaining ultrafine-grained after annealing for 1 h at 473 K and (b) becoming coarse-grained after annealing for 10 min at 563 K (Chinh et al., 2005).

respectively. Our simple model can also be used to explain the very weak sensitivity of parameter C_4 to temperature variation for $T < 0.5T_m$. At low temperatures, the annihilation of dislocations in forest dipoles is strongly facilitated by the large attractive stresses between them as they are very close to each other (their spacing equals the height of the corresponding jog), therefore the effect of temperature is limited. At high temperatures instead of dislocation pipe and grain boundary diffusion the vacancies migrate by bulk diffusion which is more temperature-dependent, because it has a larger activation energy than the former processes. As a consequence, the sensitivity of the annihilation of forest dislocations (C_4) to temperature strongly increases at high temperatures. It would be useful to develop an analytical equation to describe the temperature dependence of both the C_1 and C_4 parameters. Further investigations are needed to study the relationships shown in Fig. 9(b) in more detail. It will be the subject of further research including measurements taken at different strain rates on Al and possibly for other fcc metals.

It is noted that the strong annihilation of dislocations can explain the general instability in the microstructure of pure Al after severe plastic deformation (SPD) such as equal-channel angular pressing (ECAP) when annealing at temperatures above ~ 473 K ($0.51T_m$) (Hasegawa et al., 1999). An example of this effect can be seen in Fig. 11 for a sample of pure Al subjected to ECAP processing at room temperature to an imposed strain of ~ 8 to obtain an ultrafine-grained (UFG) structure (Chinh et al., 2005). In Fig. 11(a) the average grain size of the UFG structure remains reasonably unchanged at ~ 1.2 μm after annealing for 1 h at 473 K whereas in Fig. 11(b) the grain size strongly increases, by at least a factor of 10, when annealing at 563 K for a period of only 10 min. Thus, the UFG structure stability at low temperatures disappears very quickly when annealing at high temperatures.

4. Summary and conclusions

- (1) The plastic behavior of high purity polycrystalline aluminum was investigated over a wide range of temperatures. The experimentally measured stress–strain curves were analyzed applying a dislocation based model describing the major micro-mechanisms of plastic deformation.
- (2) It was shown for the deformation of Al at different temperatures that the interaction between forest and mobile dislocations only marginally increases the forest density compared to the effect of the interaction between mobile dislocations. Furthermore, both the trapping of mobile dislocations and the annihilation of forest dislocations are controlled by thermally-activated dislocation motion. The similarity between the two main micro-mechanisms and the negligible effect of forest dislocations on the trapping of mobile dislocations lead to a simplification of the applied theoretical model for Al over a wide range of testing temperatures.
- (3) The application of this simplified model gives an analytical relationship for the evolution of the dislocation density as a function of strain. On the basis of this function, the saturation or maximum dislocation densities were calculated for different testing temperatures.
- (4) Results of the analysis show that the microscopic parameters characterizing the multiplication and the annihilation rates of dislocations decreases and increases, respectively, with increasing testing temperature. The temperature dependence of these two microscopic quantities is interpreted qualitatively using a simple model of dislocation interaction.
- (5) Quantitative correlations between the characteristics of macroscopic and microscopic – dislocation-based – descriptions were established over a wide range of testing temperatures for pure Al, confirming the physical meaning of the phenomenological parameters describing the macroscopic evolution of the stress–strain relationships during plastic deformation.

Acknowledgments

This work was supported by the Hungarian Scientific Research Funds, OTKA, Grant No. K-81360, by the National Science Foundation of the United States under Grant No. DMR-1160966 and by the European Research Council under ERC Grant Agreement No. 267464-SPDMETALS. (TGL). The European Union and the European Social Fund provided financial support to this project under grant agreement no. TÁMOP 4.2.1./B-09/1/KMR-2010-0003.

References

- Austin, R.A., McDowell, D.L., 2011. A dislocation based constitutive model for viscoplastic deformation of fcc metals at very high strain rates. *Int. J. Plast.* 27, 1–24.
- Barlat, F., Glazov, M.V., Brem, J.C., Lege, D.J., 2002. A simple model for dislocation behavior, strain and strain rate hardening evolution in deforming aluminum alloys. *Int. J. Plast.* 18, 919–939.
- Berner, R., Kronmüller, H., 1965. *Moderne Probleme der Metallphysik*. Springer Verlag, Berlin.
- Bertin, N., Capolungo, L., Beyerlein, I.J., 2013. Hybrid dislocation dynamics based strain hardening constitutive model. *Int. J. Plast.* 49, 119–144.
- Beyerlein, I.J., Tomé, C.N., 2008. A dislocation-based constitutive law for pure Zr including temperature effects. *Int. J. Plast.* 24, 867–895.
- Chinh, N.Q., Horváth, Gy., Horita, Z., Langdon, T.G., 2004. A new constitutive relationship for the homogeneous deformation of metals over a wide range of strain. *Acta Mater.* 52, 3555–3563.
- Chinh, N.Q., Illy, J., Horita, Z., Langdon, T.G., 2005. Using the stress–strain relationships to propose regions of low and high temperature plastic deformation in aluminum. *Mater. Sci. Eng. A* 410–411, 234–238.

- Cinh, N.Q., Szommer, P., Csanádi, T., Langdon, T.G., 2006. Flow processes at low temperatures in ultrafine-grained aluminum. *Mater. Sci. Eng. A* 434, 326–334.
- Cinh, N.Q., Csanádi, T., Gubicza, J., Langdon, T.G., 2010. Plastic behavior of face-centered-cubic metals over a wide range of strain. *Acta Mater.* 58, 5015–5021.
- Csanádi, T., Cinh, N.Q., Gubicza, J., Langdon, T.G., 2011. Plastic behavior of fcc metals over a wide range of strain: macroscopic and microscopic descriptions and their relationship. *Acta Mater.* 59, 2385–2391.
- Estrin, Y., Mecking, H., 1984. A unified phenomenological description of work hardening and creep based on one-parameter models. *Acta Metall.* 32, 57–70.
- Estrin, Y., Tóth, L.S., Molinari, A., Brechet, Y., 1998. A dislocation-based model for all hardening stages in large strain deformation. *Acta Mater.* 46, 5509–5522.
- Fan, X.G., Yang, H., 2011. Internal-state-variable based self-consistent constitutive modeling for hot working of two-phase titanium alloys coupling microstructure evolution. *Int. J. Plast.* 27, 1833–1852.
- Farrokh, B., Khan, A.S., 2009. Grain size, strain rate and temperature dependence of flow stress in ultra-fine grained and nanocrystalline Cu and Al: synthesis, experiment and constitutive modeling. *Int. J. Plast.* 25, 715–732.
- Frost, H.J., Ashby, M.F., 1982. *Deformation-Mechanism Maps: The Plasticity and Creep of Metals and Ceramics*. Pergamon Press, Oxford.
- Furukawa, M., Horita, Z., Nemoto, M., Langdon, T.G., 2001. Processing of metals by equal-channel angular pressing. *J. Mater. Sci.* 36, 2835–2843.
- Gao, C.Y., Zhang, L.C., 2012. Constitutive modelling of plasticity of fcc metals under extremely high strain rates. *Int. J. Plast.* 32–33, 121–133.
- Gubicza, J., Cinh, N.Q., Lábár, J.L., Hegedűs, Z., Xu, C., Langdon, T.G., 2008. Microstructure and yield strength of severely deformed silver. *Scr. Mater.* 58, 775–778.
- Hansen, B.L., Beyerlein, I.J., Bronkhorst, C.A., Cerreta, E.K., Dennis-Koller, D., 2013. A dislocation-based multi-rate single crystal plasticity model. *Int. J. Plast.* 44, 129–146.
- Hasegawa, H., Komura, S., Utsunomiya, A., Horita, Z., Furukawa, M., Nemoto, M., Langdon, T.G., 1999. Thermal stability of ultrafine-grained aluminum in the presence of Mg and Zr additions. *Mater. Sci. Eng. A* 265, 188–196.
- Hollomon, J.H., 1945. Tensile deformation. *Trans. AIME* 162, 268–290.
- Hsiung, L.M., Lassila, D.H., 2002. Initial dislocation structure and dynamic dislocation multiplication in Mo single crystals. *Comput. Model. Eng. Sci.* 3, 185–191.
- Hughes, D.A., Hansen, N., 2000. Microstructure and strength of nickel at large strains. *Acta Mater.* 48, 2985–3004.
- Iwahashi, Y., Wang, J., Horita, Z., Nemoto, M., Langdon, T.G., 1996. Principle of equal-channel angular pressing for the ultra-fine grained materials. *Scr. Mater.* 35, 143–146.
- Iwahashi, Y., Horita, Z., Nemoto, M., Langdon, T.G., 1997. An investigation of microstructural evolution during equal-channel angular pressing. *Acta Mater.* 45, 4733–4741.
- Iwahashi, Y., Horita, Z., Nemoto, M., Langdon, T.G., 1998a. Factors influencing the equilibrium grain size in equal-channel angular pressing: role of Mg addition to aluminum. *Metall. Mater. Trans.* 29A, 2503–2510.
- Iwahashi, Y., Horita, Z., Nemoto, M., Langdon, T.G., 1998b. The process of grain refinement in equal-channel angular pressing. *Acta Mater.* 46, 3317–3331.
- Kocks, U.F., 1976. Laws for work-hardening and low-temperature creep. *J. Eng. Mater. Technol. (ASME)* 98, 76–85.
- Kocks, U.F., Mecking, H., 2003. Physics and phenomenology of strain hardening: the FCC case. *Prog. Mater. Sci.* 48, 171–273.
- Komura, S., Horita, Z., Nemoto, M., Langdon, T.G., 1999. Influence of stacking fault energy on microstructural development in equal-channel angular pressing. *J. Mater. Res.* 14, 4044–4050.
- Kovács, I., Zsoldos, L., 1973. *Dislocations and Plastic Deformation*. Akademia Publisher, Budapest.
- Kubin, L.P., Estrin, Y., 1990. Evolution of dislocation densities and the critical conditions for the Portevin-Le Chatelier effect. *Acta Metall. Mater.* 38, 697–708.
- Les, P., Stuewe, H.P., Zehetbauer, M., 1997. Hardening and strain rate sensitivity in stage IV of deformation in f.c.c. and b.c.c. metals. *Mater. Sci. Eng. A* 234–236, 453–455.
- Li, J., Soh, A.K., 2012. Modeling of plastic deformation of nanostructured materials with grain size gradient. *Int. J. Plast.* 39, 88–102.
- Li, D., Zbib, H., Sun, X., Khaleel, M., 2013. Predicting plastic flow and irradiation hardening of iron single crystal with mechanical-based continuum dislocation dynamics. *Int. J. Plast.* Available at: <<http://dx.doi.org/10.1016/j.ijplas.2013.01.015>>.
- Lim, H., Lee, M.G., Kim, J.H., Adams, B.L., Wagoner, R.H., 2011. Simulation of polycrystal deformation with grain and grain boundary effects. *Int. J. Plast.* 27, 1328–1354.
- Lukác, P., Balík, J., 1994. Kinetics of plastic deformation. *Key Eng. Mater.* 97–98, 307–322.
- Malygin, G.A., 1990. Dislocation density evolution equation and strain hardening of f.c.c. crystals. *Phys. Stat. Sol. (a)* 119, 423–436.
- Nabarro, F.R.N., Basinski, Z.S., Holt, D.B., 1964. The plasticity of pure single crystals. *Adv. Phys.* 13, 193–323.
- Nes, E., 1998. Modelling of work hardening and stress saturation in fcc metals. *Prog. Mater. Sci.* 41, 129–193.
- Roters, F., Raabe, D., Gottstein, G., 2000. Work hardening in heterogeneous alloys – a microstructural approach based on three internal state variables. *Acta Mater.* 48, 4181–4189.
- Tóth, L.S., Molinari, A., Estrin, Y., 2002. Strain hardening at large strains as predicted by dislocation based polycrystal plasticity model. *J. Eng. Mater. Technol.* 124, 71–77.
- Valiev, R.Z., Langdon, T.G., 2006. Principles of equal channel angular pressing as a processing tool for grain refinement. *Prog. Mater. Sci.* 51, 881–981.
- Valiev, R.Z., Islamgaliev, R.K., Alexandrov, I.V., 2000. Bulk nanostructured materials from severe plastic deformation. *Prog. Mater. Sci.* 45, 103–189.
- Voce, E., 1948. The relationship between stress and strain for homogeneous deformation. *J. Inst. Met.* 74, 537–562.
- Wang, Z.Q., Beyerlein, I.J., Lesar, R., 2009. Plastic anisotropy in fcc single crystals in high rate deformation. *Int. J. Plast.* 25, 26–48.
- Zehetbauer, M., 1993. Cold work hardening in stage IV and V of f.c.c. metals – II. Model fits and physical results. *Acta Mater.* 41, 589–599.
- Zehetbauer, M., Seumer, T.G., 1993. Cold work hardening in stage IV and V of f.c.c. metals – I Experiments and interpretation. *Acta Mater.* 41, 577–588.
- Zhilyaev, A.P., Langdon, T.G., 2008. Using high pressure torsion for metal processing: fundamentals and applications. *Prog. Mater. Sci.* 53, 893–979.